

## Article

# Imaging Characteristics of Disturbance Flow Field Surrounding a Hypersonic Target

Ning Chang <sup>1,2,3</sup>, Shiping Guo <sup>1,2,3,4,\*</sup>, Chunmin Zhang <sup>1,2,3</sup>, Yanqiang Wang <sup>1,2,3</sup>  and Feng Tang <sup>1,2,3</sup><sup>1</sup> School of Physics, Xi'an Jiaotong University, Xi'an 710049, China<sup>2</sup> The Institute of Space Optics, Xi'an Jiaotong University, Xi'an 710049, China<sup>3</sup> Key Laboratory for Nonequilibrium Synthesis and Modulation of Condensed Matter (Xi'an Jiaotong University), Ministry of Education, Xi'an 710049, China<sup>4</sup> State Key Laboratory of Applied Optics, Changchun Institute of Optics, Fine Mechanics and Physics, Chinese Academy of Sciences, Changchun 130033, China

\* Correspondence: guoshiping@xjtu.edu.cn

**Abstract:** The disturbance flow field arises naturally with hypersonic target flying in near space. In situations where traditional infrared and radar systems lose effectiveness, space-based optical detection of this surrounding flow can serve as an alternative method for detecting high-speed targets. This paper presents a remote sensing imaging analysis of the disturbance flow field surrounding a hypersonic target at different flight altitudes and Mach numbers. Utilizing Fourier Optics and Background-Oriented Schlieren, in conjunction with the fourth-order Runge-Kutta ray tracing algorithm, the imaging blurring and imaging deviation of three typical backgrounds under the influence of the disturbance flow field are obtained. Additionally, the study analyzes the influence of flight conditions and parameters of the imaging system on the imaging characteristics, and provides optical design recommendations. The results indicate that the presence of disturbance flow fields leads to varying degrees of visually apparent blurring effects and indiscernible deviation effects on the background images. Furthermore, the profiles of the disturbance flow field are extracted, in agreement with current experimental research. This study verifies the feasibility of space-based optical detection of hypersonic targets through disturbance flow field remote sensing imaging and contributes to the advancement of imaging research in this field.



**Citation:** Chang, N.; Guo, S.; Zhang, C.; Wang, Y.; Tang, F. Imaging

Characteristics of Disturbance Flow Field Surrounding a Hypersonic Target. *Appl. Sci.* **2023**, *13*, 8827.

<https://doi.org/10.3390/app13158827>

Received: 4 July 2023

Revised: 27 July 2023

Accepted: 28 July 2023

Published: 31 July 2023



**Copyright:** © 2023 by the authors. Licensee MDPI, Basel, Switzerland. This article is an open access article distributed under the terms and conditions of the Creative Commons Attribution (CC BY) license (<https://creativecommons.org/licenses/by/4.0/>).

**Keywords:** hypersonic target; disturbance flow field; imaging characteristic; space-based remote sensing

## 1. Introduction

Hypersonic targets in near space are characterized with high flight speed, excellent maneuverability, and great stealth; the importance of their efficient detection has been emphasized; and numerous studies on infrared [1,2] and radar [3,4] technologies for space-based and ground-based detection have been conducted. When an aircraft flies in near space at hypersonic speed, the surrounding air is violently compressed, generating a high-temperature, high-pressure, and high-density flow field [5]. The surface layers of the aircraft are ablated into gas under the effect of the high-temperature and high-pressure flow field and ionized with the surrounding air, forming a plasma sheath around the aircraft. This plasma sheath refracts and absorbs electromagnetic waves, creating challenges for radar detection [6,7]. Furthermore, the low flight trajectory of the target in near space and the curvature of the Earth also impose difficulties on radar detection. In some cases, infrared detection proves ineffective due to the aircraft's use of gliding without powered propulsion, as well as the advancements in infrared stealth materials. However, throughout the flight of the aircraft, the disturbance flow field inevitably arises, offering an opportunity for measurement and detection. The non-uniform refractive index distribution and variation of the flow field affect the transmission of target light,

resulting in the blurring and deviation of the background image [8,9]. Current mechanism analysis or experimental exploration focuses on the impact of the flow field near the optical dome of hypersonic guided missiles on the transmission of target light [10–12], which is incompatible with the optical transmission through the entire disturbance flow field.

For studying the optical transmission through the entire disturbance flow field, an effective approach is to visualize it. In April 2011, October 2014, February 2015, and December 2018, NASA [13] conducted a series of flight tests against the desert flora below 10 km and visualized the disturbance flow field of single and dual transonic aircraft through Background-Oriented Schlieren, respectively. The Background-Oriented Schlieren (BOS) technique is a flow visualization method based on the deflection of light after passing through the flow field, and measures the variation of the flow field density by computer image processing, with the advantages of the simple optical system, ensuring easy and fast measurement. Currently, the BOS technique is mainly applied to the parameter measurement of flow fields [14,15], flow visualization [16], and the optical system transfer function measurement [17]. NASA has indeed visualized the flow field, but its flight tests were conducted for transonic aircraft at altitudes below 10 km and at Mach number approximately 1.0 Ma, where the atmospheric components and conditions are quite different from those of hypersonic aircraft in near space [18]. Additionally, NASA has not disclosed specific details about their experiments, and it is also difficult to perform BOS experiments in near space. Therefore, it is essential to investigate the imaging characteristics of the disturbance flow field surrounding hypersonic targets.

This paper presents a comprehensive investigation into the imaging characteristics of the disturbance flow field. The disturbance flow field of a hypersonic target under diverse flight conditions was simulated using the computational fluid dynamics software ANSYS Fluent. Ray tracing was performed utilizing the fourth-order Runge-Kutta algorithm, enabling the calculation of essential optical parameters, such as refractive index gradients, phase differences, and deflection angles. Moreover, the imaging blurring and imaging deviation were analyzed against three representative backgrounds (desert, ocean, and city) using Fourier Optics and Background-Oriented Schlieren techniques. Subsequently, the correlation between imaging blurring, imaging deviation, and the orbit height, pixel size, and focal length of the space-based imaging detection system was established. The results demonstrate that the presence of perturbed flow fields leads to a varying degrees of visually perceptible blurring effects and indiscernible deviation effects in the background image under different flight conditions. The profiles of the disturbance field were successfully extracted from the deviated image, demonstrating the feasibility of detecting hypersonic targets through the disturbance flow field. This approach holds promise as an alternative scheme in situations where infrared and radar detection methods are not available.

The remainder of this paper is organized as follows. In Section 2, the research method of imaging characteristics of the disturbance flow field surrounding a hypersonic target based on Fourier Optics and Background-Oriented Schlieren was analyzed. In Section 3, the results of the imaging blurring and imaging deviation caused by the disturbance flow field were demonstrated, and the influence mechanism of the relevant parameters was analyzed. In Section 4, the conclusions drawn from the study were presented.

## 2. Methods

### 2.1. Flow Density Calculation

The disturbance flow field of a 2D conical target was simulated using the computational fluid dynamics software ANSYS Fluent [10]. The target's geometric model was generated in Auto CAD and then imported into ANSYS ICEM CFD for meshing. The majority of the grid quality values were found to be greater than 0.8, which meets the CFD calculation standard. Figure 1 displays the geometric model of the target used in the simulations. The CFD calculations of the disturbance flow field were performed under different flight conditions, as detailed in Table 1. The RANS solver was employed to calculate the mean density distribution  $\rho(x, y, z)$  of the disturbance flow field, as depicted in Figure 2a.

**Table 1.** Flight conditions.

Figure Serial Number	Flight Altitude (km)	Mach Number
(a)	20	10
(b)	30	8
(c)/(e)	30	10
(d)	30	12
(f)	50	10

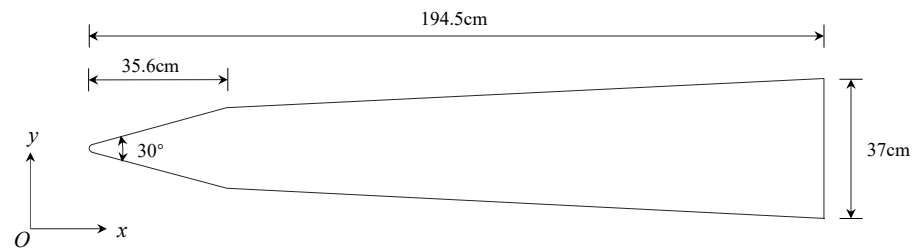


**Figure 1.** The geometry model of target.

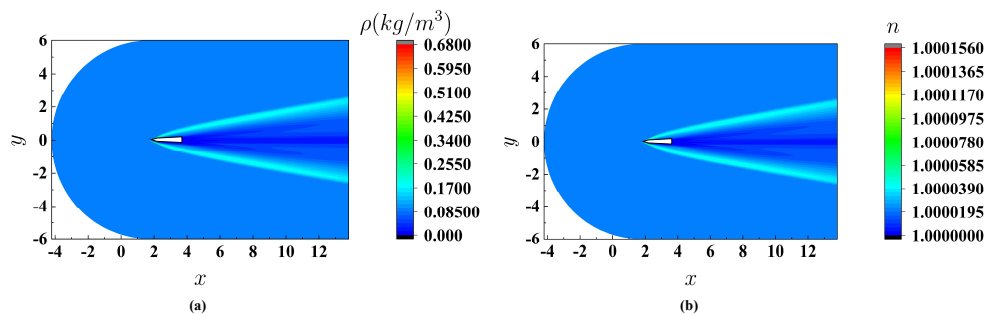


**Figure 2.** The density and refractive index distribution of the disturbance flow field: Flight altitude = 20 km; Mach number = 10 Ma; (a) density distribution; (b) refractive distribution.

**2.2. Flow Refractive Index Computation and Ray Tracing Algorithm**

The refractive index of the flow can be derived from the flow density via the Gladstone–Dale relationship [19]

$$n = 1 + \rho K_{GD} \tag{1}$$

where  $n$  is the refractive index,  $\rho$  is the density in  $\text{kg}/\text{m}^3$ , and  $K_{GD}$  is a coefficient which can be expressed as [8]

$$K_{GD} = 2.23 \times 10^{-4} \left( 1 + \frac{7.52 \times 10^3}{\lambda^2} \right) \tag{2}$$

where  $\lambda$  is the light wavelength in nm, and  $K_{GD}$  varies weakly with the wavelength. The refractive index field calculated by Equation (2) is shown in Figure 2b, where  $\lambda$  is selected as 532 nm.

The propagating path of light in any medium with a nonuniform distribution of the refractive index can be expressed by ray equation [8]

$$\frac{d}{ds} \left( n \frac{dr}{ds} \right) = \nabla n \tag{3}$$

where  $s$  is the arc length of the ray propagation path,  $\mathbf{r}$  is the position vector of the ray propagation, and  $\nabla n$  is the refractive index gradient. Under the assumption of the ray vector  $\mathbf{T} = n(\mathbf{dr}/ds)$ , Equation (3) can be expressed as first-order differential equations.

$$\begin{cases} \frac{d\mathbf{T}}{ds} = \nabla n \\ \frac{d\mathbf{r}}{ds} = \frac{\mathbf{T}}{n} \end{cases} \quad (4)$$

Equation (4) can only be solved analytically when the refractive index satisfies a particular distribution. The approximate solution for the disturbance flow field with random changes the in refractive index is typically obtained by numerical solutions. By introducing a new parameter  $dt = ds/n$ , Equation (4) can be expressed as

$$\begin{cases} \frac{d\mathbf{T}}{dt} = n(\nabla n) = f(t, \mathbf{T}) \\ \frac{d\mathbf{r}}{dt} = \mathbf{T} = n[\cos \alpha, \cos \beta, \cos \gamma] = g(t, \mathbf{r}) \end{cases} \quad (5)$$

where  $\alpha$ ,  $\beta$ , and  $\gamma$  are the angles between the light and the  $x$ -axis,  $y$ -axis, and  $z$ -axis, respectively.

Assuming  $\mathbf{D}(\mathbf{r}) = n\nabla n$ , the fourth order Runge–Kutta method [20] could be carried out to solve Equation (5). The approximate solution is expressed as

$$\begin{cases} \mathbf{T}_{i+1} = \mathbf{T}_i + \frac{h}{6}(\mathbf{K}_1 + 2\mathbf{K}_2 + 2\mathbf{K}_3 + \mathbf{K}_4) \\ \mathbf{r}_{i+1} = \mathbf{r}_i + \frac{h}{6}(\mathbf{L}_1 + 2\mathbf{L}_2 + 2\mathbf{L}_3 + \mathbf{L}_4) \end{cases} \quad (6)$$

$\mathbf{K}_j$  and  $\mathbf{L}_j$   $j = (1, 2, 3, 4)$  can be obtained by

$$\begin{cases} \mathbf{K}_1 = f(t_i, \mathbf{T}_i) = \mathbf{D}(\mathbf{r}_i) \\ \mathbf{L}_1 = g(t_i, \mathbf{r}_i) = \mathbf{T}_i \end{cases} \quad (7)$$

$$\begin{cases} \mathbf{K}_2 = f\left(t_i + \frac{h}{2}, \mathbf{T}_i + \frac{h}{2}\mathbf{K}_1\right) = \mathbf{D}\left(\mathbf{r}_i + \frac{h}{2}\mathbf{T}_i\right) \\ \mathbf{L}_2 = g\left(t_i + \frac{h}{2}, \mathbf{r}_i + \frac{h}{2}\mathbf{L}_1\right) = \mathbf{T}_i + \frac{h}{2}\mathbf{D}(\mathbf{r}_i) \end{cases} \quad (8)$$

$$\begin{cases} \mathbf{K}_3 = f\left(t_i + \frac{h}{2}, \mathbf{T}_i + \frac{h}{2}\mathbf{K}_2\right) = \mathbf{D}\left(\mathbf{r}_i + \frac{h}{2}\mathbf{T}_i + \frac{h^2}{4}\mathbf{D}(\mathbf{r}_i)\right) \\ \mathbf{L}_3 = g\left(t_i + \frac{h}{2}, \mathbf{r}_i + \frac{h}{2}\mathbf{L}_2\right) = \mathbf{T}_i + \frac{h}{2}\mathbf{D}\left(\mathbf{r}_i + \frac{h}{2}\mathbf{T}_i\right) \end{cases} \quad (9)$$

$$\begin{cases} \mathbf{K}_4 = f(t_i + h, \mathbf{T}_i + h\mathbf{K}_3) = \mathbf{D}\left(\mathbf{r}_i + h\mathbf{T}_i + \frac{h^2}{2}\mathbf{D}(\mathbf{r}_i)\right) \\ \mathbf{L}_4 = g(t_i + h, \mathbf{r}_i + h\mathbf{L}_3) = \mathbf{T}_i + h\mathbf{D}\left(\mathbf{r}_i + \frac{h}{2}\mathbf{T}_i + \frac{h^2}{4}\mathbf{D}(\mathbf{r}_i)\right) \end{cases} \quad (10)$$

The Runge–Kutta method for ray tracing is described by Equations (7)–(10), where  $h$  is the step length. If the initial position vector  $\mathbf{r}_0 = (x_0, y_0, z_0)$ , ray vector  $\mathbf{T}_0 = n[\cos \alpha_0, \cos \beta_0, \cos \gamma_0]$  and step length  $h$  were specified, the propagation path of the light can be obtained by iterating Equations (6)–(10). Considering the axisymmetry of the model, the two-dimensional refractive index field can be transformed into a three-dimensional refractive index field for ray tracing. It is crucial to calculate the gradient of the refractive index at each point in the disturbance flow field to facilitate the ray tracing procedure. The gradient of the refractive index  $\nabla n$  can be calculated using the Barron gradient operator [21]

$$\begin{cases} \frac{\partial n(i,j,k)}{\partial x} = \frac{1}{12\Delta x} (n(i-2, j, k) - 8n(i-1, j, k) + 8n(i+1, j, k) - n(i+2, j, k)) \\ \frac{\partial n(i,j,k)}{\partial y} = \frac{1}{12\Delta y} (n(i, j-2, k) - 8n(i, j-1, k) + 8n(i, j+1, k) - n(i, j+2, k)) \\ \frac{\partial n(i,j,k)}{\partial z} = \frac{1}{12\Delta z} (n(i, j, k-2) - 8n(i, j, k-1) + 8n(i, j, k+1) - n(i, j, k+2)) \end{cases} \quad (11)$$

As mesh nodes cannot contain every point in the disturbance flow field, it is required to interpolate the refractive index or refractive index gradient using the distance-weighted averaged interpolation algorithm with the 8 nearest nodes, which can be expressed as [22]

$$n_j = \frac{\sum_{i=1}^8 n_i \prod_{\substack{j \neq i \\ j=1}}^8 d_j}{\sum_{i=1}^8 \prod_{\substack{j \neq i \\ j=1}}^8 d_j} \tag{12}$$

$$d_j = \sqrt{(x - x_j)^2 + (y - y_j)^2 + (z - z_j)^2} \tag{13}$$

### 2.3. Phase Difference and Imaging Blurring Derivation

As light propagates through the disturbance flow field, the optical distance through which it passes can be expressed by the optical path length [23]

$$\text{OPL} = \sum_i n_i h \tag{14}$$

where  $n_i$  is the refractive index at  $r_i$  and  $h$  is the step length of ray tracing. The optical path difference of the light can be used to evaluate the phase difference and can be expressed as [23]

$$\text{OPD} = \text{OPL} - \text{OPL}_0 \tag{15}$$

where  $\text{OPL}_0$  is the optical path length that the light propagates in free space. Thus, the phase difference can be expressed as [23]

$$\varphi(x, y) = \frac{2\pi}{\lambda} \text{OPD} \tag{16}$$

where  $\lambda$  is the wavelength of light.

The pupil function can be determined by calculating the phase difference generated by all rays on the image plane and can be expressed as [24]

$$P(x, y) = \begin{cases} A(x, y)e^{i\varphi(x, y)} & x^2 + y^2 \leq (D/2)^2 \\ 0 & x^2 + y^2 \geq (D/2)^2 \end{cases} \tag{17}$$

where  $A(x, y)$  is the amplitude distribution and  $D$  is the diameter of the pupil.

According to the Huygens principle, the far-field approximation of the amplitude distribution of light waves within the pupil of the light on the image plane is expressed as [24]

$$U(x', y') = \iint P(x, y)e^{-i\frac{2\pi}{\lambda f'}(xx' + yy')} dx dy \tag{18}$$

where  $f'$  is the focal length of the optical system. Apparently,  $U(x', y')$  is the Fourier transform of  $P(x, y)$ . The point spread function can be expressed as [24]

$$\text{PSF}(x', y') = |U(x', y')|^2 \tag{19}$$

Applying the Fourier transform to the point spread function, the optical transfer function OTF can be obtained [24]

$$\text{OTF}(f_{x'}, f_{y'}) = \iint \text{PSF}(x', y')e^{-i2\pi(f_{x'}x' + f_{y'}y')} dx' dy' \tag{20}$$

The amplitude distribution of the image plane can be expressed as [24]

$$I(x_0, y_0) = O(x_0, y_0) * \text{PSF}(x', y') \tag{21}$$

where  $O(x_0, y_0)$  is the amplitude distribution of the object plane,  $*$  represents the convolution.

The peak signal-to-noise ratio is used to evaluate the quality between blurred image and original image and can be expressed as [25]

$$\text{PSNR}(i, j) = 10 \log_{10} \left[ \frac{(L - 1)^2}{\text{MSE}(i, j)} \right] \tag{22}$$

where  $L$  is the maximum valid value for a pixel, MSE is the mean squared error of the image and can be expressed as [25]

$$\text{MSE}(i, j) = \frac{1}{MN} \sum_{i=1}^M \sum_{j=1}^N [f(i, j) - \hat{f}(i, j)]^2 \tag{23}$$

where  $\hat{f}(i, j)$  and  $f(i, j)$  represent the blurred image and the original image, respectively.  $M$  and  $N$  represent the length and width of the image, respectively.

#### 2.4. Background-Oriented Schlieren and Imaging Deviation Computation

Background-Oriented Schlieren (BOS) uses the deflection of light to identify changes in the refractive index (or density) of a flow field. When light passes through the disturbance flow field, it undergoes deflection from its original path, causing a shift in the position of the light incident on the CCD camera. This shift results in a disparity between the background images captured by the CCD camera in the presence of a disturbance flow field (referred to as the experimental image) and in its absence (referred to as the reference image) [26]. In this study, Background-Oriented Schlieren is employed for the imaging deviation analysis.

Figure 3 illustrates the schematic of Background-Oriented Schlieren (BOS) [26]. In the figure,  $Z_O$  represents the distance from the background to the center of the disturbance flow field,  $W$  denotes the length of the disturbance flow field,  $Z_B$  corresponds to the distance between the background and the camera lens, and  $Z_I$  signifies the distance from the lens to the imaging plane, which is approximately equal to the focal length  $f$ . The dotted line in the figure represents the path of light in the absence of a disturbance flow field, while the solid line depicts the actual path of light propagation through the disturbance flow field. The  $y$ -direction deflection angle between these two rays is denoted by  $\varepsilon_y$ . The parameter  $\Delta y$  represents the displacement in the  $y$  direction between the corresponding point on the reference image and the experimental image.  $\Delta y'$  denotes the virtual shift of  $\Delta y$  relative to the background. Similarly,  $\varepsilon_x$  represents the deflection angle in the  $x$  direction,  $\Delta x$  is the displacement in the  $x$  direction, and  $\Delta x'$  is the virtual displacement of  $\Delta x$ .

After ray tracing, the  $x$  direction deflection angle and  $y$  direction deflection angle can be expressed as [26]

$$\varepsilon_x = \int_{Z_O-W/2}^{Z_O+W/2} \frac{1}{n} \frac{\partial n}{\partial x} dz \quad \varepsilon_y = \int_{Z_O-W/2}^{Z_O+W/2} \frac{1}{n} \frac{\partial n}{\partial y} dz \tag{24}$$

Based on the geometry in the diagram, the relationship between  $\Delta x'$  and  $\Delta x$  and  $\Delta y'$  and  $\Delta y$  can be expressed as [26]

$$\frac{\Delta x'}{Z_B} = \frac{\Delta x}{f} \quad \frac{\Delta y'}{Z_B} = \frac{\Delta y}{f} \tag{25}$$

For minimal deflection angle, it can be expressed approximately as [26]

$$\varepsilon_x = \frac{\Delta x'}{Z_O} = \frac{Z_B \Delta x}{Z_O f} \quad \varepsilon_y = \frac{\Delta y'}{Z_O} = \frac{Z_B \Delta y}{Z_O f} \tag{26}$$

Thus, the displacement can be expressed as [26]

$$\Delta x = \varepsilon_x \frac{Z_O f}{Z_B} \quad \Delta y = \varepsilon_y \frac{Z_O f}{Z_B} \tag{27}$$

The corresponding pixel shift on the CCD plane can be expressed as

$$\Delta u = \frac{\Delta x}{a} = \varepsilon_x \frac{Z_O f}{a Z_B} \quad \Delta v = \frac{\Delta y}{a} = \varepsilon_y \frac{Z_O f}{a Z_B} \tag{28}$$

where  $a$  is the pixel size of CCD. The relationship between the gray value of the deviated image and the original image satisfies [27]

$$I_o(x + \Delta u, y + \Delta v) = I_d(x, y) \tag{29}$$

Using the given image as the original image  $I_o$ , and the displacement field  $\Delta u, \Delta v$  as the displacement label, the deviated image  $I_d$  can be generated using interpolation.

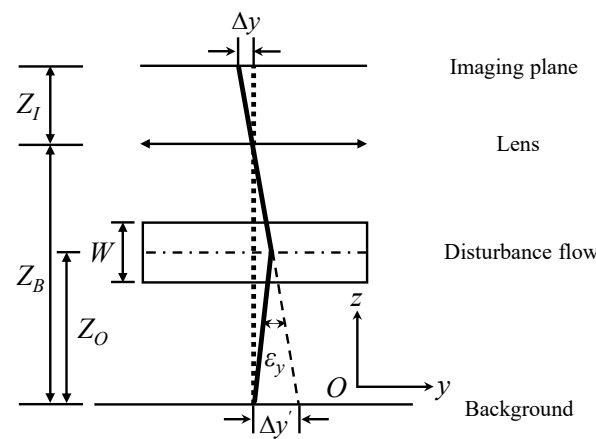


Figure 3. The schematic diagram of BOS.

Imaging characteristics of blurring and deviation were performed utilizing an ideal optical system with the parameters listed in Table 2.

Table 2. The parameters of an ideal optical system for imaging.

Parameters	Value
Orbit height (km)	400
Focal length (m)	1.0
Pixel size (μm)	5
Array size	1024 × 1024
Diameters of pupil (m)	0.2
Detect wavelength (nm)	532

### 3. Results and Discussion

#### 3.1. The Results of Imaging Blurring

The initial position vector  $r_0$  is fixed at the bottom of the disturbance flow field, and the incident rays are along the positive  $z$  axis. The phase difference after ray tracing is obtained by Equation (16). Figure 4 shows the distribution of the phase difference under different flight conditions.

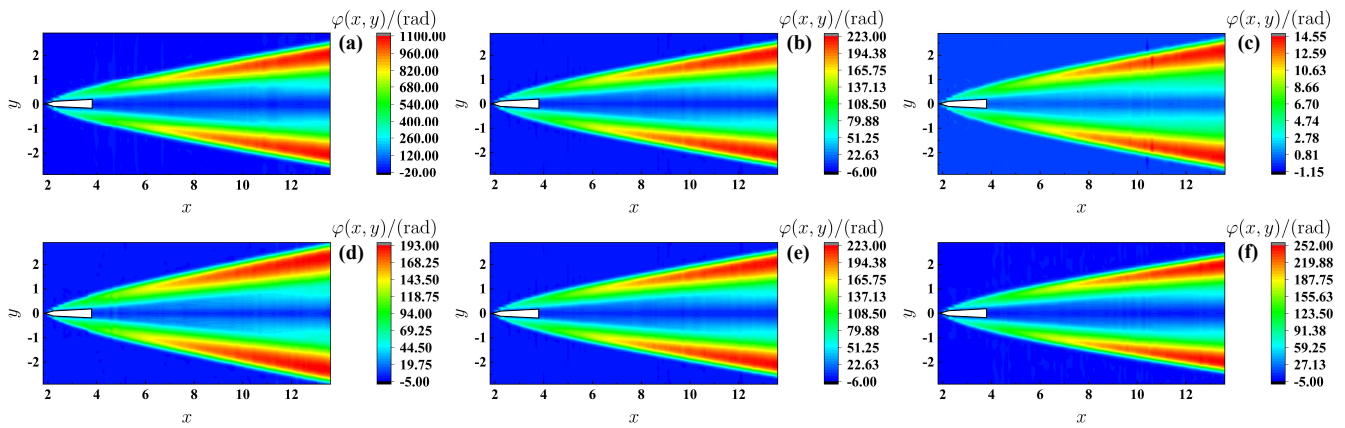


**Figure 4.** The phase difference distribution of disturbance flow field: Refer to Table 1 for flight conditions from (a–f).

The phase difference exhibits a decreasing trend with an increasing flight altitude due to the thinning of the atmosphere at higher altitudes, resulting in a reduction of the refractive index and optical path difference of light. Similarly, as the Mach number progressively rises, the atmosphere experiences enhanced compression, leading to an augmentation in the phase difference. The phase difference is influenced by the density and refractive index distribution within the disturbance flow field. Specifically, a higher degree of fluctuation in the refractive index distribution along the propagation path corresponds to a larger optical path difference of the light. Remarkably larger values of the phase difference are symmetrically distributed downstream of the disturbance flow field, where the disturbance flow field extends extensively, consequently inducing larger optical path differences. The negative phase difference arises due to the comparatively lower atmospheric density in the wake of the target compared to free space, which aligns with the principles of fluid dynamics.

Figures 5–7 show the results of imaging blurring, which were computed using Equation (21), against three typical backgrounds: desert, ocean, and city. In comparison to the corresponding original images Figures 5–7, the resultant images exhibit varying degrees of blurriness, and as the flight altitude increases, the background noise gradually diminishes. The stark contrast observed between the resultant images and their original counterparts significantly enhances the identification of space-based remote sensing images.

Reference	20km 10Ma	30km 8Ma	30km 10Ma	30km 12Ma	50km 10Ma

**Figure 5.** The results of imaging blurring over desert.

Reference	20km 10Ma	30km 8Ma	30km 10Ma	30km 12Ma	50km 10Ma

**Figure 6.** The results of imaging blurring over ocean.

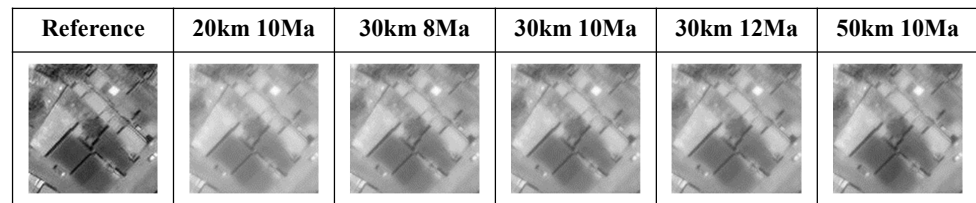


**Figure 7.** The results of imaging blurring over city.

As presented in Table 3, the Peak Signal-to-Noise Ratio (PSNR) is computed for each image to provide a more accurate quantification of the degree of imaging blurring. The results reveal that across three typical backgrounds, the PSNR demonstrates an improvement with increasing flight altitude and Mach number. In reference to Figure 4, at a Mach number of 12, the phase difference attains its maximum value of 252.0 rad, accompanied by a wave aberration of  $40.1\lambda$ . However, the disturbance flow field area is found to be the smallest within the detection range, leading to results that contradict the phase difference trend. This discrepancy can be attributed to fluid dynamics, where the angle of the shock wave decreases as the Mach number increases, subsequently resulting in the smallest flow field area at 12 Ma within the detection range.

**Table 3.** PSNR of imaging blurring varies with flight altitude and Mach number.

PSNR/dB	20 km	30 km			50 km
	10 Ma	8 Ma	10 Ma	12 Ma	10 Ma
Desert	9.23251	9.93444	9.98668	10.12562	10.81715
Ocean	13.35157	14.90093	15.34042	15.72033	16.66509
City	14.61291	16.59343	17.15776	17.67577	19.56554

### 3.2. The Results of Imaging Deviation

According to Table 2 and Figure 3, the distance from the background to the center of the disturbance flow field, denoted as  $Z_O$ , corresponds to the flight altitude and is set at 20 km, 30 km, and 50 km, respectively. The length of disturbance flow field  $W$  is 6 m. The distance from the background to the camera lens  $Z_B$  is the orbit height and is set to 400 km. The pixel size of the CCD camera is  $5 \mu\text{m}$  and the focal length of the camera lens is 1.0 m.

Figures 8 and 9 show the results of the  $x$  direction and  $y$  direction deflection angles under different flight conditions calculated by Equations (24)–(28), where the positive value represents the positive deflection towards  $x$  or  $y$  direction, while the negative value represents the opposite direction. Apparently, as flight altitude increases, the deflection angle decreases, and as the Mach number increases, the deflection angle increases, which follows the same pattern as the phase difference. In addition, the  $y$  direction deflection angle is an order of magnitude greater than the  $x$  direction, indicating that the former has a more pronounced influence on the imaging deviation. The deflection angle is also affected by the density or refractive index distribution of the disturbance flow field. The greater the fluctuation in the refractive index distribution along the path of propagation, the larger the deflection angle of light. The larger values of the deflection angle are similarly symmetrical in the downstream of the disturbance flow field. When specifying the Mach number or flight altitude, the disturbance flow field attains its highest density at 20 km or 12 Ma, resulting in the greatest imaging deviation.

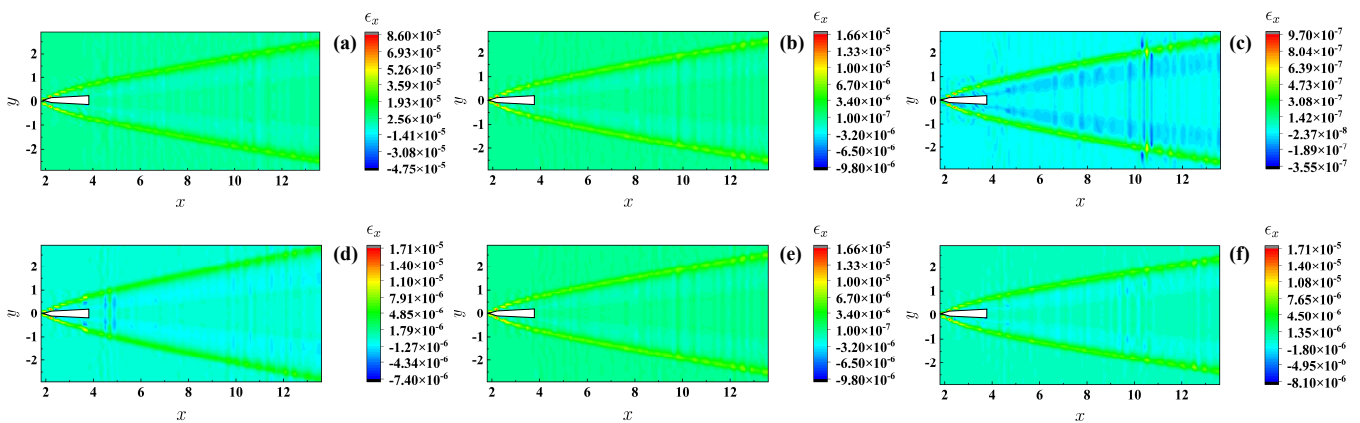


**Figure 8.** The  $x$  direction deflection angle distribution: Refer to Table 1 for flight conditions from (a–f).

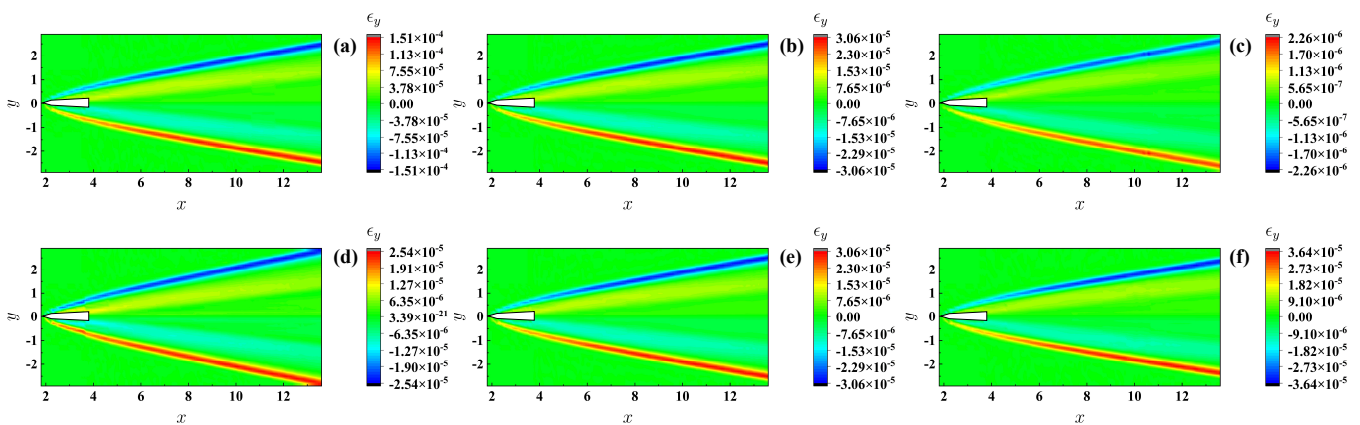


**Figure 9.** The  $y$  direction deflection angle distribution: Refer to Table 1 for flight conditions from (a–f).

The pixel shift is calculated by dividing the displacement by the CCD pixel size. The displacement results indicate that the majority of the pixel shifts are at the sub-pixel level. Figures 10–12 illustrate the imaging deviation results, based on the pixel shift, for the desert, ocean, and city backgrounds, respectively. For comparison with the natural background, Figure 13 demonstrates imaging deviation with a speckle pattern as the background. Although no significant visual difference is observed between the deviated image and the original image, the profile of the disturbance flow field can be extracted through background subtraction. The profiles of the disturbance flow field, shown in the last row of Figures 10–13, are found to be consistent with the existing experimental studies. These profiles can provide insights into the presence of a hypersonic target in flight, serving as an alternative method for hypersonic target detection. It is evident that the imaging deviation is influenced by the background image, with a more speckled background image retaining more information about the extracted disturbance flow field. In addition, according to the Gladstone–Dale relationship, the refractive index proves to be insensitive to wavelength variation, allowing for the utilization of the infrared band for nighttime imaging. Table 4 presents the Peak Signal-to-Noise Ratio (PSNR) of imaging deviation, which varies with flight altitude and Mach number. In contrast to imaging blurring, PSNR of imaging deviation demonstrates an increasing trend with flight altitude, yet slightly decreases with Mach number, and is several magnitudes larger.

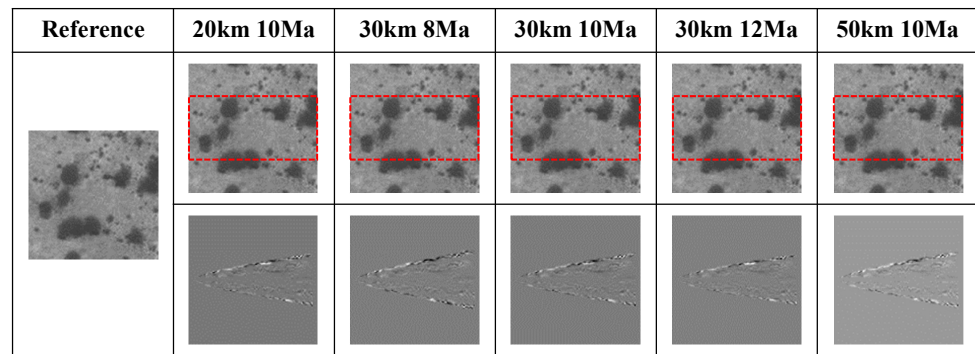


**Figure 10.** The results of imaging deviation over desert: The last row is the difference between the deviated image and the original image; the red dashed box indicates the location of the disturbance flow field.

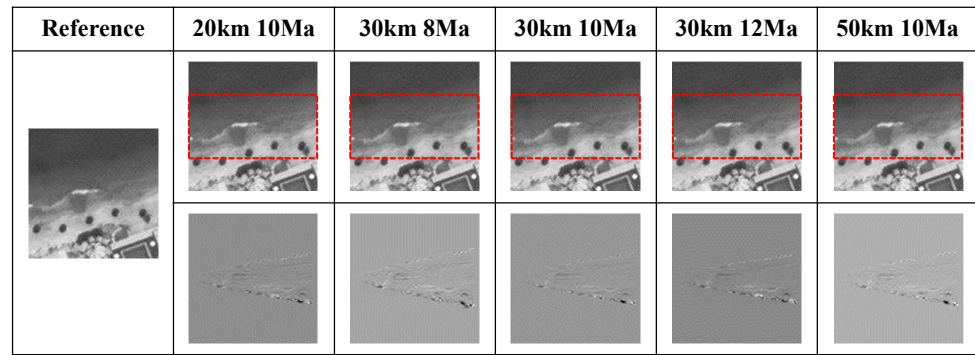


**Figure 11.** The results of imaging deviation over ocean: The last row is the difference between the deviated image and the original image; the red dashed box indicates the location of the disturbance flow field.

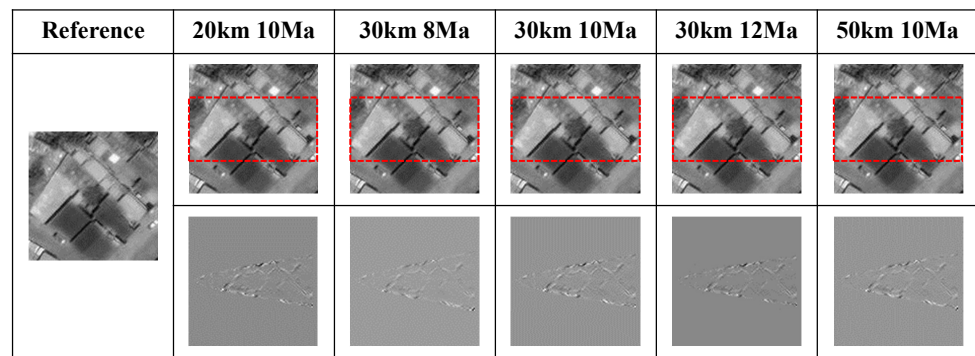


**Figure 12.** The results of imaging deviation over city: The last row is the difference between the deviated image and the original image; the red dashed box indicates the location of the disturbance flow field.

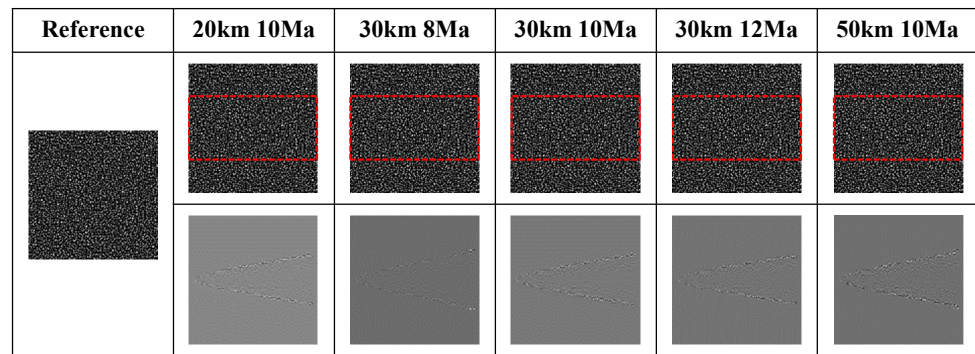


**Figure 13.** The results of imaging deviation over speckle: The last row is the difference between the deviated image and the original image; the red dashed box indicates the location of the disturbance flow field.

As stated in Equation (28) and mentioned previously, the imaging deviation is influenced by several factors, including the deflection angles  $\epsilon$ , focal length  $f$ , orbit height  $Z_B$ , flight altitude  $Z_O$  and pixel size  $a$ . However, the influence of deflection angles and flight altitude on imaging deviation is mutually constrained. As the flight altitude increases, the atmospheric density becomes sparser, leading to a significant reduction in the deflection angles. Moreover, the magnitude of the decrease in deflection angles far surpasses that of the increase in flight altitude. Additionally, flight altitude is often uncontrollable; thus, our primary focus is on exploring the impact of other parameters on imaging deviation. It is observed that a lower orbit height leads to a larger pixel shift; however, it also reduces the detection range. Therefore, selecting a low orbit or sun-synchronous orbit for detection is deemed appropriate.

**Table 4.** PSNR of imaging deviation varies with flight altitude and Mach number.

PSNR/dB	20 km	30 km			50 km
	10 Ma	8 Ma	10 Ma	12 Ma	10 Ma
Desert	46.42771	57.55659	56.69947	55.65402	83.28530
Ocean	46.82656	58.70044	56.70328	56.40288	78.51409
City	42.09763	53.03142	52.52691	51.28720	73.28530

Figure 14 shows the effect of pixel size and focal length on  $y$  direction pixel shift under different flight conditions. When the focal length is specified, the pixel shift in the  $y$  direction increases as the pixel size decreases, whereas when the pixel size is specified, the pixel shift in the  $y$  direction increase as the focal length increases. Meanwhile, the influence of flight altitude and Mach number on the pixel shift remains consistent with the previously discussed trends. To achieve an image that preserves more deviation characteristics, the camera necessitates a large focal length and a small pixel size. However, it is crucial to acknowledge that both focal length and pixel size cannot be adjusted indefinitely. Increasing the focal length leads to a larger camera system volume, which may pose challenges for the satellite and escalate research and development costs. Conversely, decreasing the pixel size results in a reduction of luminous flux, and there exists a trade-off between these two parameters. Hence, a comprehensive consideration of the system requirements and constraints is essential when determining the optimal focal length and pixel size for the camera.

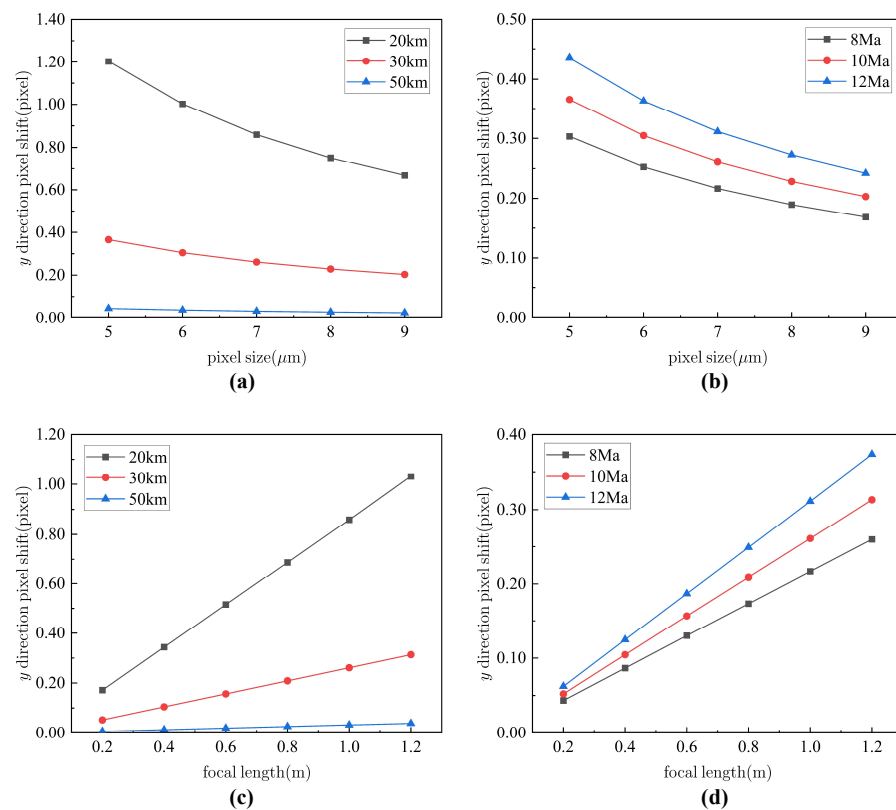


**Figure 14.** The influence of pixel size and focal length on  $y$  direction pixel deviation: (a) the influence of pixel size under different flight altitudes where the focal length is 1.0 m; (b) the influence of pixel size under different Mach numbers where the focal length is 1.0 m; (c) the influence of focal length under different flight altitudes where the pixel size is 5  $\mu\text{m}$ ; (d) the influence of focal length under different Mach numbers where the pixel size is 5  $\mu\text{m}$ .

#### 4. Summary

In this study, we have thoroughly examined the remote sensing imaging of the disturbance flow field surrounding a hypersonic target under five different flight conditions. Utilizing Fourier Optics and Background-Oriented Schlieren techniques, we have presented imaging blurring and deviation against three typical backgrounds. The imaging quality has been evaluated using the Peak Signal-to-Noise Ratio (PSNR). We have quantitatively analyzed the influences of flight conditions and imaging system parameters on the imaging characteristics. The key findings of our investigation are as follows: The disturbance flow field significantly impacts the background images, resulting in varied degrees of blurring and deviation. The extracted profiles of the disturbance flow field from the deviated images are in accordance with current experimental studies. As the flight altitude increases, the phase difference and deflection angle decrease, leading to a reduced blurring of the images and higher PSNR, owing to the lower atmospheric density at higher altitudes. Conversely, as the Mach number increases, the phase difference and deflection angle increase due to the greater compression of the atmosphere surrounding the hypersonic target. However, the degree of image blurring decreases due to the larger flow field area. The majority of pixel shifts in imaging deviation are at the sub-pixel level, making them indistinguishable to the naked eye. Nevertheless, the profile of the flow field can be extracted from the deviated images. The imaging deviation is closely related to the focal length, pixel size, and orbit height of the space-based imaging system. Our quantitative analysis highlights the importance of a space-based imaging system with a large focal length and a small pixel size, while a low orbit or sun-synchronous orbit is preferred. The imaging results confirm the feasibility of detecting hypersonic targets through disturbance flow field imaging, providing an alternative detection approach when

traditional infrared and radar systems lose effectiveness. Moreover, the remote sensing detection of the flow field profile around hypersonic targets not only contributes to the field of high-speed target detection but also enables an in-depth analysis and optimization of the performance and flight characteristics of hypersonic targets. This research also offers theoretical support for experimental studies in this area.

**Author Contributions:** Conceptualization, C.Z. and S.G.; methodology, S.G.; software, N.C. and S.G.; formal analysis, N.C., S.G., C.Z., Y.W. and F.T.; investigation, F.T.; data curation, N.C.; writing—original draft preparation, N.C.; writing—review and editing, N.C., S.G. and C.Z.; supervision, C.Z.; funding acquisition, C.Z. All authors have read and agreed to the published version of the manuscript.

**Funding:** This research was funded by the Major International (Regional) Joint Research Project of National Natural Science Foundation of China (42020104008); The Key Program of National Natural Science Foundation of China (41530422); Shaanxi Fundamental Science Research Project for Mathematics and Physics (22JSZ007); National High Technology Research and Development Program of China (863 Program) (2012AA121101); The General Program of National Natural Science Foundation of China (61775176); Shaanxi Province Key Research and Development Program of China (2021GXLH-Z-058); National Natural Science Foundation of China (62005221); Open Foundation of the State Key Laboratory of applied optics (SKLAO2021001A04).

**Institutional Review Board Statement:** Not applicable.

**Informed Consent Statement:** Not applicable.

**Data Availability Statement:** Data sharing is not applicable to this article.

**Conflicts of Interest:** The authors declare no conflict of interest.

## References

1. Candler, G.V.; Leyva, I.A. Computational Fluid Dynamics Analysis of the Infrared Emission from a Generic Hypersonic Glide Vehicle. *Sci. Glob. Secur.* **2022**, *30*, 117–130. [\[CrossRef\]](#)
2. Zhao, J.; Hong, Q.; Hu, S.; Ye, Q.; Liu, Z. Simulation analysis of space-based infrared remote sensing characteristics of hypersonic vehicles. In Proceedings of the AOPC 2022: Infrared Devices and Infrared Technology; and Terahertz Technology and Applications, Beijing, China, 18–20 December 2022; Gong, H., Lu, J., Eds.; International Society for Optics and Photonics; SPIE: Bellingham, DC, USA, 2023; Volume 12555, p. 125550A.
3. Yuan, L.; Xiangyu, Z.; Zhong, Y.; Dachao, H.; Shuliang, D. Sine tracking model of hypersonic target in near space based on radar detecting. In Proceedings of the IET International Radar Conference 2015, Hangzhou, China, 14–16 October 2015; pp. 1–4.
4. Sun, Z.; Li, X.; Cui, G.; Yi, W.; Kong, L. Hypersonic Target Detection and Velocity Estimation in Coherent Radar System Based on Scaled Radon Fourier Transform. *IEEE Trans. Veh. Technol.* **2020**, *69*, 6525–6540. [\[CrossRef\]](#)
5. Navó, A.; Bergada, J. Aerodynamic Study of the NASA's X-43A Hypersonic Aircraft. *Appl. Sci.* **2020**, *10*, 8211. [\[CrossRef\]](#)
6. Anderson, J. *Hypersonic and High-Temperature Gas Dynamics*; AIAA education Series; American Institute of Aeronautics and Astronautics: Reston, VA, USA, 2006.
7. Zhao, Z.; Bai, B.; Yuan, K.; Tang, R.; Xiong, J.; Wang, K. Effect of Terahertz Antenna Radiation in Hypersonic Plasma Sheaths with Different Vehicle Shapes. *Appl. Sci.* **2022**, *12*, 1811. [\[CrossRef\]](#)
8. Yin, X. *Principle of Aero-Optics*; China Astronautics Publishing House: Beijing, China, 2003.
9. Ding, H.; Yi, S.H.; Xu, Y.; Zhao, X.H. Recent developments in the aero-optical effects of high-speed optical apertures: From transonic to high-supersonic flows. *Prog. Aerosp. Sci.* **2021**, *127*, 100763. [\[CrossRef\]](#)
10. Xu, L.; Cai, Y. Influence of altitude on aero-optic imaging deviation. *Appl. Opt.* **2011**, *50*, 2949–2957. [\[CrossRef\]](#) [\[PubMed\]](#)
11. Zhao, X.; Yi, S.; Ding, H. Experimental study on the influence of attitude angle on the aero-optical effects of a hypersonic optical dome. *Optik* **2020**, *201*, 163448. [\[CrossRef\]](#)
12. Wu, Y.; Xue, W.; Xu, L.; Yao, Y.; Zhao, S.; Li, N. Optimized Least-squares Support Vector Machine for Predicting Aero-optic Imaging Deviation Based on Chaotic Particle Swarm Optimization. *Optik* **2019**, *206*, 163215. [\[CrossRef\]](#)
13. Heineck, J.; Banks, D.; Smith, N.; Schairer, E.; Bean, P.; Robillos, T. Background-Oriented Schlieren Imaging of Supersonic Aircraft in Flight. *AIAA J.* **2020**, *59*, 11–21. [\[CrossRef\]](#)
14. Ohno, H.; Toya, K. Localized gradient-index field reconstruction using background-oriented schlieren. *Appl. Opt.* **2019**, *58*, 7795. [\[CrossRef\]](#) [\[PubMed\]](#)
15. Sun, Z.; Miao, X.; Jagadeesh, C. Experimental investigation of the transonic shock-wave/boundary-layer interaction over a shock-generation bump. *Phys. Fluids* **2020**, *32*, 106102. [\[CrossRef\]](#)
16. Ramanah, D.; Raghunath, S.; Mee, D.J.; Rösger, T.; Jacobs, P.A. Background oriented schlieren for flow visualisation in hypersonic impulse facilities. *Shock Waves* **2007**, *17*, 65–70. [\[CrossRef\]](#)

17. Goldhahn, E.; Seume, J. The background oriented schlieren technique: Sensitivity, accuracy, resolution and application to a three-dimensional density field. *Exp. Fluids* **2007**, *43*, 241–249. [[CrossRef](#)]
18. Yan, T.; Langille, J.; Ward, W.; Gault, W.; Scott, A.; Bell, A.; Touahiri, D.; Zheng, S.H.; Zhang, C. A compact static birefringent interferometer for the measurement of upper atmospheric winds: concept, design and lab performance. *Atmos. Meas. Tech.* **2021**, *14*, 6213–6232. [[CrossRef](#)]
19. Merzkirch, W. *Flow Visualization*; Academic Press: Cambridge, MA, USA, 1987.
20. Qiao, Y. *Gradient Index Optics*; Science Press: Beijing, China, 1991.
21. Barron, J.; Fleet, D.; Beauchemin, S. Performance Of Optical Flow Techniques. *Int. J. Comput. Vis.* **1994**, *12*, 43–77. [[CrossRef](#)]
22. Shepard, D. A two-dimensional interpolation function for irregularly-spaced data. In Proceedings of the 1968 23rd ACM National Conference, New York, NY, USA, 27–29 August 1968; pp. 517–524.
23. Born, M.; Born, L.; Wolf, E.; Born, M.; Bhatia, A.; Clemmow, P.; Gabor, D.; Stokes, A.; Taylor, A.; Wayman, P.; et al. *Principles of Optics: Electromagnetic Theory of Propagation, Interference and Diffraction of Light*; Cambridge University Press: Cambridge, UK, 1999.
24. Goodman, J. *Introduction to Fourier Optics*; McGraw-Hill Physical and Quantum Electronics Series; W. H. Freeman: New York, NY, USA, 2005.
25. Hore, A.; Ziou, D. Image quality metrics: PSNR vs. SSIM. In Proceedings of the 2010 20th International Conference on Pattern Recognition, Istanbul, Turkey, 23–26 August 2010; IEEE: Piscataway, NJ, USA, 2010; pp. 2366–2369.
26. Venkatakrisnan, L.; Meier, G. Density measurements using the background oriented schlieren technique. *Exp. Fluids* **2004**, *37*, 237–247. [[CrossRef](#)]
27. Wang, G.; Zhang, L.; Yao, X. StrainNet-3D: Real-time and robust 3-dimensional speckle image correlation using deep learning. *Opt. Lasers Eng.* **2022**, *158*, 107184. [[CrossRef](#)]

**Disclaimer/Publisher’s Note:** The statements, opinions and data contained in all publications are solely those of the individual author(s) and contributor(s) and not of MDPI and/or the editor(s). MDPI and/or the editor(s) disclaim responsibility for any injury to people or property resulting from any ideas, methods, instructions or products referred to in the content.